

# Ultrabroadband, Large Sensitivity Position Sensitivity Detector Based on a $\text{Bi}_2\text{Te}_{2.7}\text{Se}_{0.3}/\text{Si}$ Heterojunction and Its Performance Improvement by Pyro-Phototronic Effect

Shuang Qiao, Mingjing Chen, Yu Wang, Jihong Liu,\* Junfeng Lu, Fangtao Li, Guangsheng Fu, Shufang Wang,\* Kailiang Ren,\* and Caofeng Pan\*

$\text{Bi}_2\text{Te}(\text{Se})_3$ , as a novel topological insulator, is a prospective candidate for next-generation spintronic and photoelectric devices. Here, A series of  $\text{Bi}_2\text{Te}_{2.7}\text{Se}_{0.3}$  films are successfully prepared on Si substrate with different thicknesses and used as a self-powered light position sensitive detector (PSD) through the introduction of a lateral photovoltaic effect (LPE). Owing to its wide and strong absorption, the high surface mobility of the  $\text{Bi}_2\text{Te}_{2.7}\text{Se}_{0.3}$  layer, and the outstanding heterojunction quality, this PSD shows an unprecedentedly broadband photoresponse from  $\approx 350$  to  $\approx 2200$  nm and exhibits very good performance with ultralarge sensitivities ( $283.71 \text{ mV mm}^{-1}$  at 532 nm,  $137.4 \text{ mV mm}^{-1}$  at 1064 nm,  $38.91 \text{ mV mm}^{-1}$  at 1550 nm, and  $16.56 \text{ mV mm}^{-1}$  at 2200 nm), perfect nonlinearity ( $<3\%$ ), and ultrafast response times ( $\approx 52.1 \mu\text{s}/\approx 70.2 \mu\text{s}$ ), all of which are among or represent the best results reported until now, especially in the infrared region. Additionally, its sensitivity can also be greatly improved through the addition of a bias voltage with an increment up to 194.6% at  $-1$  V. More importantly, the pyro-phototronic effect, which can be used to modulate both the LPE and the time response, is surprisingly observed in this PSD but with different working mechanisms than found in traditional photodetectors.

## 1. Introduction

Topological insulators (TI), as a novel quantum state of matter, have attracted increasingly interest in physics, materials, and electronics due to their insulating or semiconductor properties in bulk but with metal surface states in the band edge.<sup>[1–3]</sup> Recently, it was found that some TIs even exhibit a wonderful spin-momentum coupling induced by chiral charge carriers and Dirac-cone-based gapless surface states, thus the spin quantum Hall effect can be found in them without applying external magnetic field due to the quantized charge and spin conductance.<sup>[4,5]</sup> Among all these TIs,  $\text{Bi}_2\text{Te}_3$ , and  $\text{Bi}_2\text{Se}_3$  have gathered significant attention because of their relatively large bulk bandgap of about 0.3 eV, which makes them great potential application in room-temperature broadband spintronic or photoelectric devices.<sup>[1,6,7]</sup> Moreover, a strong optical absorption and a special warping

effect can be aroused in them over a wide spectral range caused by the Dirac-like surface state,<sup>[8–10]</sup> which can be further used to enhance the performances of the devices. Meanwhile, it has been reported that the excitation of ultrafast laser pulses can result in a transient population of carriers at both the unoccupied surface state and the empty conduction band of the TIs.<sup>[11,12]</sup> The suitable bandgap, strong optical absorption, unique warping effect, and fast dynamical response, which are all special properties of the  $\text{Bi}_2\text{Te}_3$  or  $\text{Bi}_2\text{Se}_3$ , enable it as a prospective candidate for the new-generation ultrafast broadband optoelectronic devices. However, from previous results, high-performance devices usually need to combine with other materials to fully exert their synergistic effect. Therefore, researchers have been trying best to seek for different TI-based heterostructures, and some heterojunctions (e.g., graphene/ $\text{Bi}_2\text{Te}_3$ ,<sup>[13]</sup> graphene/ $\text{Bi}_2\text{Se}_3$ ,<sup>[14]</sup>  $\text{SnSe}/\text{Bi}_2\text{Te}_3$ ,<sup>[15]</sup>  $\text{WS}_2/\text{Bi}_2\text{Te}_3$ ,<sup>[16]</sup>  $\text{Bi}_2\text{Te}_3/\text{GaAs}$ ,<sup>[17]</sup> and even  $\text{Bi}_2\text{Te}_3/\text{Bi}_2\text{Se}_3$ <sup>[18]</sup>) have already been successfully prepared, and demonstrated to show very good photoelectric performances. However, these structures are relatively complex with tedious preparation techniques and small working size, in contrast, architecture of TI/Si heterojunction may be more tempting as Si is still leading in the industrial

Prof. S. Qiao, Y. Wang, Prof. J. Liu, Prof. G. Fu, Prof. S. Wang  
Hebei Key Laboratory of Optic-Electronic Information and Materials  
National & Local Joint Engineering Laboratory of New Energy  
Photoelectric Devices

College of Physics Science and Technology, Hebei University  
Baoding 071002, P. R. China  
E-mail: liujihong@hbu.edu.cn; sfwang@hbu.edu.cn

Dr. M. Chen  
College of Quality and Technical Supervision  
Hebei University  
Baoding 071002, P. R. China

Dr. J. Lu, F. Li, Prof. K. Ren, Prof. C. Pan  
Beijing Key Laboratory of Micro-Nano Energy and Sensor  
Beijing Institute of Nanoenergy and Nanosystems, Chinese Academy of  
Sciences  
Beijing 100083, P. R. China  
E-mail: renkailiang@binn.cas.cn; cfpan@binn.cas.cn

Prof. K. Ren, Prof. C. Pan  
School of Nanoscience and Technology  
University of Chinese Academy of Sciences  
Beijing 100049, P. R. China

 The ORCID identification number(s) for the author(s) of this article can be found under <https://doi.org/10.1002/aelm.201900786>.

DOI: 10.1002/aelm.201900786

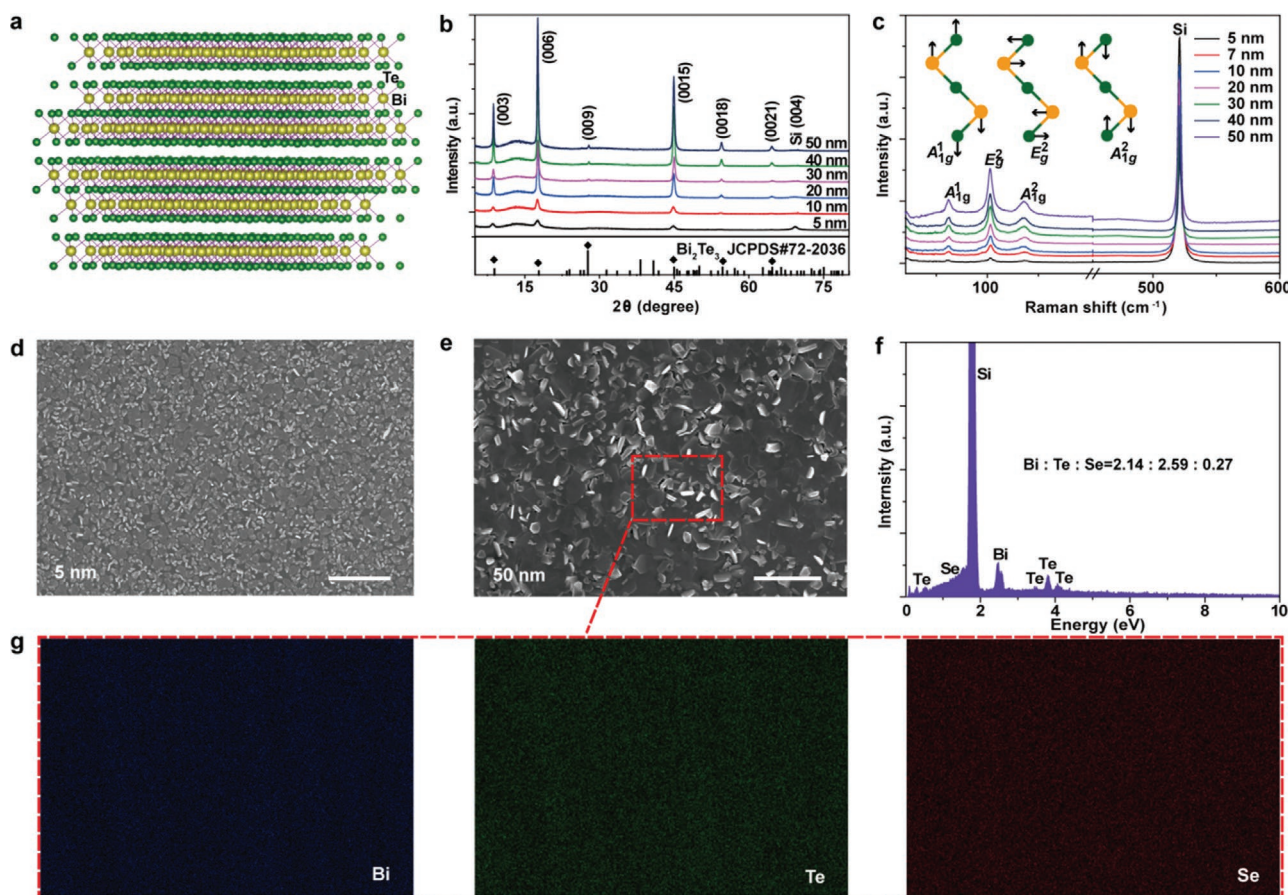


**Figure 1.** a) Illustration of the layered  $\text{Bi}_2\text{Te}(\text{Se})_3$  crystal structure. b) XRD and c) Raman results of the  $\text{Bi}_2\text{Te}_{2.7}\text{Se}_{0.3}$  films. SEM surface morphology of the  $\text{Bi}_2\text{Te}_{2.7}\text{Se}_{0.3}$  films with thicknesses of d) 5 nm and e) 50 nm, respectively. f) EDX spectroscopy and g) the Bi, Te, Se elemental mapping results.

optoelectronic or photovoltaic community because of its high abundance and mature technology process. Besides,  $\text{Bi}_2\text{Te}_3$  and  $\text{Bi}_2\text{Se}_3$  are all stoichiometric rhombohedral materials with quintuple stacked layered structure and relatively weak layer-to-layer van der Waals coupling,<sup>[19]</sup> as shown in **Figure 1a**. Therefore, high-quality thin films can be easily deposited on the Si substrate via different techniques,<sup>[20–27]</sup> making further basic studies and potential applications possible. More importantly, it was suggested that the construction of  $\text{Bi}_2\text{Se}_3$  on Si could introduce a very high Schottky barrier of  $\approx 0.34$  eV at the interface,<sup>[22,28,29]</sup> which can be used to accelerate the separation of photo-excited carriers in Si or  $\text{Bi}_2\text{Se}_3$  and inhibit their recombination simultaneously, thus the outstanding photoelectric responses were usually obtained.

On account of these advantages, till now, the high-quality  $\text{Bi}_2\text{Se}_3/\text{Si}$  or  $\text{Bi}_2\text{Te}_3/\text{Si}$  heterostructures have been successfully prepared by several groups and exploited as ultrafast broadband photodetectors (PDs).<sup>[21–23,25,27]</sup> However, for traditional PDs, researchers mainly concentrated on the longitudinal separation of photo-generated carriers in the interface of the heterojunctions, while the excellent surface transport properties were usually neglected or not well utilized. In particular,  $\text{Bi}_2\text{Te}_3$  and  $\text{Bi}_2\text{Se}_3$  have been observed to show an extremely high surface mobility<sup>[30]</sup> and indicated to be excellent electrode materials as well as graphene.<sup>[31]</sup> Therefore, novel or new working principle detectors are

urgently needed to develop. Fortunately, besides PDs, TI/Si heterostructures may also show promising potential in light position sensitive detector (PSD) by introducing lateral photovoltaic effect (LPE), which not only needs longitudinal separation and transport of the photo-excited carriers, but also requires surface transverse diffusion of the separated carriers subsequently,<sup>[32–34]</sup> thus may maximize the properties of the TI/Si heterojunctions. However, till now, the related studies on the LPE response are absent in this heterostructure; the carrier separation, electrical transport, and the corresponding LPE mechanism still remain unclear. More importantly, it has been predicted that the TIs can achieve very wide photodetection in a range from the visible even to terahertz frequencies due to their suitable bandgap and metal surface state, thus the TI/Si heterojunction-based PSD may greatly break through the photoresponse range of the previously reported PSDs.

In this paper, the LPE in the  $\text{Bi}_2\text{Te}_{2.7}\text{Se}_{0.3}/\text{Si}$  heterojunctions was well studied. This heterostructure shows very excellent LPE performances with unprecedented working range ( $\approx 350$  to  $\approx 2200$  nm), ultralarge sensitivity ( $283.71 \text{ mV mm}^{-1}$ ,  $137.4 \text{ mV mm}^{-1}$ ,  $38.91 \text{ mV mm}^{-1}$ , and  $16.56 \text{ mV mm}^{-1}$  at typical 532, 1064, 1550, and 2200 nm, respectively), perfect non-linearity ( $< 3\%$ ), ultrafast response times ( $\approx 52.1 \mu\text{s}$ / $\approx 70.2 \mu\text{s}$ ), and without needing any external power. Besides, when a bias voltage is applied on the heterojunction, the LPE response can also be largely improved due to the modulation of the built-in

field at the interface. More importantly, the pyro-phototronic effect is observed in this heterojunction, however, the photoresponse only enhances at the laser on stage but keeps constant at the laser off stage, which is quite different from the traditional PDs. Based on their different working mechanisms, these results are well explained. This work indicates that the TI-based heterostructures hold promising application in extraordinary broadband infrared PSD devices.

## 2. Results and Discussion

The crystal structure as well as the phase purity of the  $\text{Bi}_2\text{Te}_{2.7}\text{Se}_{0.3}/\text{Si}$  heterojunctions was determined by using X-ray diffraction (XRD), as shown in Figure 1b. It is clear that only six diffraction peaks identified as  $(00n)$  ( $n = 3, 6, 9, 15, 18, 21$ ) can be obtained besides the  $(004)$  peak of the Si substrate, suggesting that the as-prepared  $\text{Bi}_2\text{Te}_{2.7}\text{Se}_{0.3}$  films should be exclusively indexed to the rhombohedral  $\text{Bi}_2\text{Te}_3$  crystal geometry (JCPDS: 72–2036) and has a  $c$ -axis preferred orientation. Besides, the high resolution transmission electron microscopy (HRTEM) was also measured to further quantify the quality of the heterojunctions, as shown in Figure S1, Supporting Information. An amorphous  $\text{SiO}_2$  layer is obtained at the surface of the Si substrate with thickness of  $\approx 2$  nm, but the  $\text{Bi}_2\text{Te}_{2.7}\text{Se}_{0.3}$  film still unambiguously exhibits the layered structure with very good crystal quality. More importantly, a well-defined interface is obtained between the  $\text{Bi}_2\text{Te}_{2.7}\text{Se}_{0.3}$  film and the  $\text{SiO}_2$  layer, indicating the naturally strong layer-by-layer growth characteristic of the  $\text{Bi}_2\text{Te}_{2.7}\text{Se}_{0.3}$ . Figure 1c gives the Raman results of the  $\text{Bi}_2\text{Te}_{2.7}\text{Se}_{0.3}$  films. Besides the Si vibration peak at  $\approx 520$   $\text{cm}^{-1}$ , three prominent vibration peaks are

found at 62.1, 102.4, and 135.5  $\text{cm}^{-1}$ , which can be identified as the out-of-plane  $A_{1g}^1$ , the in-plane  $E_g^2$ , and the out-of-plane  $A_{2g}^1$  peaks of the  $\text{Bi}_2\text{Te}_{2.7}\text{Se}_{0.3}$  films, respectively.<sup>[35]</sup> The surface morphology of the  $\text{Bi}_2\text{Te}_{2.7}\text{Se}_{0.3}$  films was determined by scanning electron microscopy (SEM), with images of different films shown in Figure 1d,e and Figure S2, Supporting Information, respectively. The  $\text{Bi}_2\text{Te}_{2.7}\text{Se}_{0.3}$  nanoplates can be found on the Si substrate at the beginning with relatively small size and sparse distribution, and then become interconnected with gradually increased nanoplate size and thickness. The atomic force microscopy (AFM) measurements suggest that the surfaces of the films are relatively smooth with the averaged roughness of  $\approx 1$  nm (Figure S3, Supporting Information). In order to quantify the composition and elemental distribution of the  $\text{Bi}_2\text{Te}_{2.7}\text{Se}_{0.3}$  films, energy dispersive X-ray spectroscopy (EDXS) and element mapping have been measured, as shown in Figure 1f,g. The Bi, Te, and Se elements are all homogeneously distributed on the selected area with nominal atomic ratio of Bi:Te:Se  $\approx 2.14:2.59:0.27$ , which is in accordance with the composition of the composite target.

Prior to the LPE measurements, the surface transverse current–voltage ( $I$ – $V$ ) characteristics were first estimated, and the linear behaviors could be gotten in all the films, ruling out the possible contact effect of the Au electrodes, as shown in Figure 2a. Then, the longitudinal electrical properties were measured in the  $\text{Bi}_2\text{Te}_{2.7}\text{Se}_{0.3}/\text{Si}$  heterojunction, with  $I$ – $V$  results of a typical 10 nm sample shown in Figure 2b. The curve shows very good diode characteristics, indicating a Schottky contact is formed between the  $\text{Bi}_2\text{Te}_{2.7}\text{Se}_{0.3}$  film and the Si substrate. Besides, the heterojunction exhibits a substantial photoreponse with photocurrent gradually increasing with adding the laser power even to 30 mW for a 532 nm laser illumination.

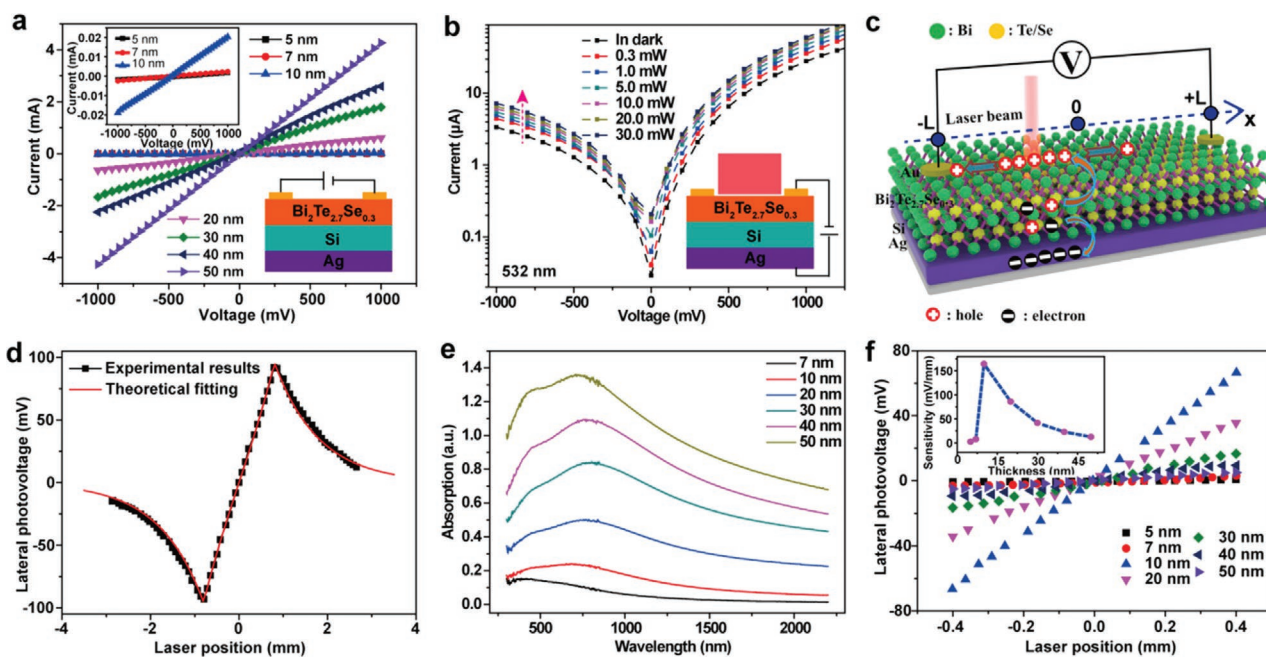


**Figure 2.** a) Transverse  $I$ – $V$  curves of the heterojunctions with different  $\text{Bi}_2\text{Te}_{2.7}\text{Se}_{0.3}$  film thicknesses. b) Longitudinal  $I$ – $V$  curves of the 10 nm-thickness  $\text{Bi}_2\text{Te}_{2.7}\text{Se}_{0.3}/\text{Si}$  heterojunction in dark and under different powers illumination. c) Schematic illustration of the LPE in the  $\text{Bi}_2\text{Te}_{2.7}\text{Se}_{0.3}/\text{Si}$  heterojunction. d) A typical laser position-dependent LPV curve. e) The absorption spectra of the  $\text{Bi}_2\text{Te}_{2.7}\text{Se}_{0.3}$  films on glass substrates. f) LPV curves of the heterojunctions with different  $\text{Bi}_2\text{Te}_{2.7}\text{Se}_{0.3}$  thicknesses under 5 mW illumination of a 532 nm laser with inset the extracted sensitivities.

Figure 2c shows the structure and LPE measurement diagram of the  $\text{Bi}_2\text{Te}_{2.7}\text{Se}_{0.3}/\text{Si}$  heterojunction. For LPE, when a laser beam is perpendicularly illuminated on the  $\text{Bi}_2\text{Te}_{2.7}\text{Se}_{0.3}$  side, electron-hole pairs can be excited, and swept to the top and bottom layers by the interface field, then the separated holes in the  $\text{Bi}_2\text{Te}_{2.7}\text{Se}_{0.3}$  layer will diffuse from illuminated position to non-illuminated regions due to density gradient, thus a lateral photovoltage (LPV), which is linearly proportional to the laser position, is generated between the Au electrodes (here the lateral shift of the transmitted beam and the surface plasmon polariton was not considered<sup>[36–38]</sup>). With laser beam changing from left (/right) electrode to right (/left) electrode, a position-dependent LPV curve is gotten, as shown in Figure 2d. According to the diffusion theory of separated carriers, the LPV can be well deduced, with equation expressed as follows<sup>[39–41]</sup>

$$\begin{aligned} \text{LPV}(x) &= \kappa (N_{\text{Left}} - N_{\text{Right}}) \\ &= \kappa N_0 \left[ \exp\left(-\frac{|x-L|}{l_0}\right) - \exp\left(-\frac{|x+L|}{l_0}\right) \right] \end{aligned} \quad (1)$$

where  $\kappa$  represents a constant coefficient,  $N_{\text{Left}}$  and  $N_{\text{Right}}$  are the hole densities collected by the left electrode and the right electrode, respectively,  $L$  represents their half-distance,  $N_0$  represents the amount of holes separated into the  $\text{Bi}_2\text{Te}_{2.7}\text{Se}_{0.3}$  layer, and  $l_0$  is the diffusion length of holes. Based on Equation (1), the laser position-dependent LPV result can be perfectly fitted, further confirming the diffusion theory model of the LPE. To determine the spectral response of the  $\text{Bi}_2\text{Te}_{2.7}\text{Se}_{0.3}$  films, the absorption spectrums are investigated by using the ultraviolet-visible spectrophotometer, as shown in Figure 2e. It is observed that the  $\text{Bi}_2\text{Te}_{2.7}\text{Se}_{0.3}$  films exhibit a very wide absorption spanning from  $\approx 350$  nm even to  $\approx 2200$  nm and the absorption

intensity increases with film thickness, demonstrating the great prospect of this heterostructure for a broadband photo-detection. Figure 2f gives the LPV curves of the  $\text{Bi}_2\text{Te}_{2.7}\text{Se}_{0.3}/\text{Si}$  heterojunctions with a typical 5 mW illumination of a 532 nm laser. The LPE response exhibits a strong dependence on the film thickness as the extracted sensitivity improves greatly from  $2.55 \text{ mV mm}^{-1}$  to a maximum of  $164.7 \text{ mV mm}^{-1}$  with the  $\text{Bi}_2\text{Te}_{2.7}\text{Se}_{0.3}$  thickness increasing from 3 to 10 nm, and then starts to decrease gradually to  $12.52 \text{ mV mm}^{-1}$  for the 50 nm-thickness  $\text{Bi}_2\text{Te}_{2.7}\text{Se}_{0.3}$  heterojunction, as shown in Figure 2f (the inset result). This phenomenon can be well understood as the separation, transport, and diffusion of the photo-generated carriers are all playing a vital role in the LPE response.<sup>[42,43]</sup> With the  $\text{Bi}_2\text{Te}_{2.7}\text{Se}_{0.3}$  thickness increasing until to an ultimate value, the depletion region gets broadened gradually, leading to an enhancement of the depletion layer, and thus the quickly improved separation efficiency.<sup>[42,43]</sup> When the thickness exceeds the ultimate value, the depletion region nearly keeps constant by increasing the  $\text{Bi}_2\text{Te}_{2.7}\text{Se}_{0.3}$  thickness again. However, the recombination and back tunneling probabilities become increasingly large due to the increased transport and diffusion distance of the separated carriers (from the depletion layer to the surface and also to the electrodes), therefore, the LPE response turns to reduce with further increasing the  $\text{Bi}_2\text{Te}_{2.7}\text{Se}_{0.3}$  thickness for the  $\text{Bi}_2\text{Te}_{2.7}\text{Se}_{0.3}/\text{Si}$  heterostructure.

Then, the LPE response of the 10 nm-thick  $\text{Bi}_2\text{Te}_{2.7}\text{Se}_{0.3}/\text{Si}$  heterojunction is well investigated. Figure 3a,d gives the LPV curves of a 532 nm laser and a 1064 nm laser, respectively, under illumination of different powers. The well linear relationships are observed in the whole power range and the LPE response enhances clearly with illumination power extending from 0.1 mW even to 60 mW for both lasers, indicating the wide spectra and the large power response range of this

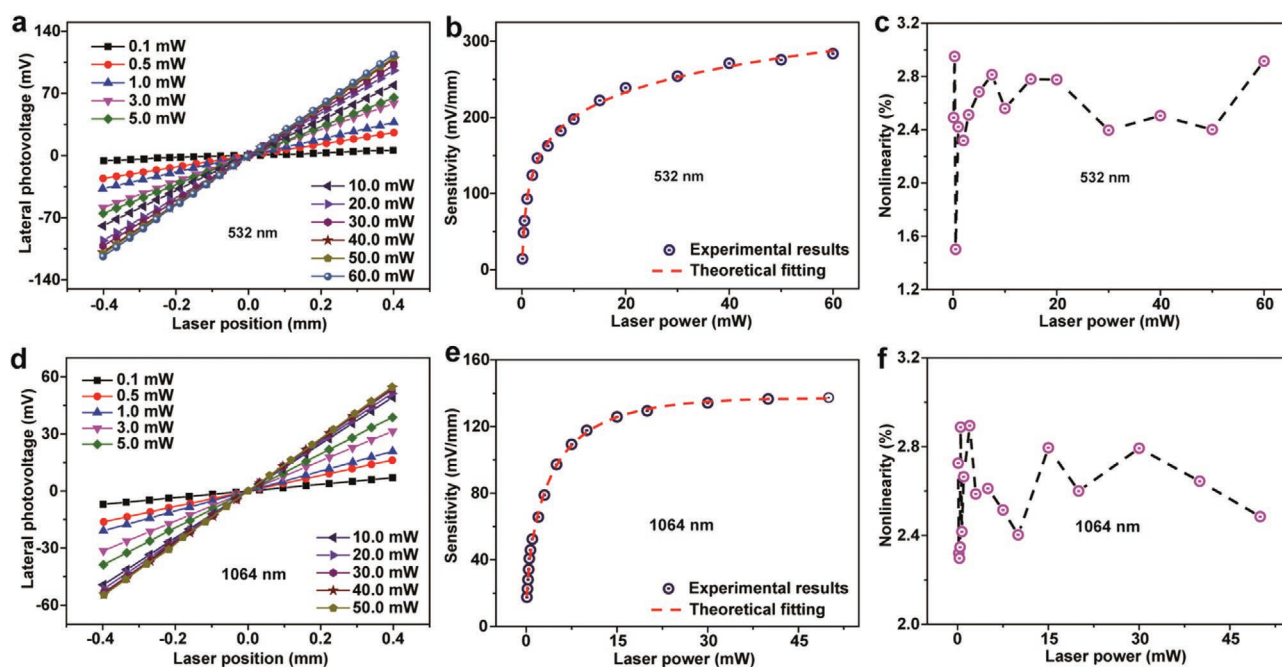


**Figure 3.** LPV curves under different powers illumination of a) 532 and d) 1064 nm lasers, respectively. The extracted power-dependent sensitivities for b) 532 and e) 1064 nm, respectively. The calculated power-dependent nonlinearities for c) 532 nm and f) 1064, respectively.

heterojunction. To well evaluate the LPE responses, linear fitting is performed to extract the key parameter of sensitivity, as summarized in Figure 3b,e. The sensitivity improves from 14.25 mV mm<sup>-1</sup> to a near-saturation of 283.71 mV mm<sup>-1</sup> as power changes from 0.1 to 60 mW for the 532 nm laser, and it enhances from 16.53 mV mm<sup>-1</sup> to 137.4 mV mm<sup>-1</sup> as power changes from 0.1 to 50 mW for the 1064 nm laser. Apparently, the increasing rates of the sensitivities are all very fast in low powers but become gradually slow in high powers, which can be ascribed to the progressively raised recombination velocity.<sup>[44–46]</sup> Moreover, the whole sensitivity of the 1064 nm is less than that of the 532 nm. There are mainly two reasons for this phenomenon: one is the higher absorption in visible range than that in near-infrared range for this heterojunction, as shown in Figure 2e; the other is that the recombination velocity of the photo-excited carriers in the Bi<sub>2</sub>Te<sub>2.7</sub>Se<sub>0.3</sub> layer is faster than that in the Si substrate due to its smaller carrier lifetime,<sup>[47,48]</sup> which can be directly reflected from the changing rate of the power-dependent sensitivities. As the laser energy of both 532 and 1064 nm is mainly absorbed by the Bi<sub>2</sub>Te<sub>2.7</sub>Se<sub>0.3</sub> layer in low powers, thus the sensitivity of the 532 nm has nearly the same increasing rate as that of the 1064 nm. However, different from that of the 1064 nm laser, more photons, that penetrate the Bi<sub>2</sub>Te<sub>2.7</sub>Se<sub>0.3</sub> layer, can be absorbed by the Si substrate for the 532 nm laser in high powers, resulting in its larger sensitivity and slower saturation.

Till now, the LPE has been observed in many different materials, but the largest working wavelength is still no more than 1064 nm, which is mainly due to their unsuitable bandgap and limited absorption range.<sup>[32–34,39–46,49–56]</sup> However, different from these materials, Bi<sub>2</sub>Te<sub>2.7</sub>Se<sub>0.3</sub> is a very narrow gap semiconductor

and has been predicted to show great application in broadband infrared photodetections.<sup>[8]</sup> From Figure 2e, it is indicated that the absorption range of the Bi<sub>2</sub>Te<sub>2.7</sub>Se<sub>0.3</sub> layer can be extended even to 2200 nm, thus this heterojunction may particularly break through the wavelength limit. Therefore, to further unfold the working range, the LPV curves were measured under other two lasers' illumination of 1550 and 2200 nm, as shown in Figure 4a,c. Though the LPE response is much lower as compared with that of the 1064 nm and decreases quickly with increasing laser wavelength (which can be mainly ascribed to their different light absorptions shown in Figure 2e), the well linear relationship can still be obtained, and the LPE response also improves gradually with enhancing laser intensity. The sensitivities are deduced and summarized in Figure 4b,d. Similar as that of the 1064 nm, the sensitivity increases quickly at first and then slowly to a saturation of 38.91 mV mm<sup>-1</sup> and 16.56 mV mm<sup>-1</sup> for 1550 and 2200 nm, respectively.

To well account for the laser power-dependent sensitivity in the Bi<sub>2</sub>Te<sub>2.7</sub>Se<sub>0.3</sub>/Si heterojunction, the sensitivity expression is deduced on the basis of Equation (1) as follows<sup>[39–41]</sup>

$$\text{Sensitivity} = \frac{2\kappa N_0}{l_0} \exp\left(-\frac{L}{l_0}\right) (-L \leq x \leq L) \quad (2)$$

$N_0$  is suggested to be related to both power ( $P$ ) and wavelength ( $\lambda$ ) with the expression of  $N_0 = \eta \left(\frac{P\lambda}{hc}\right)^\delta$ , where  $\eta$  and  $\delta$  are the effective factors ( $0 < \eta, \delta < 1$ ),  $h$  and  $c$  represent the Planck coefficient and the vacuum light velocity, respectively,

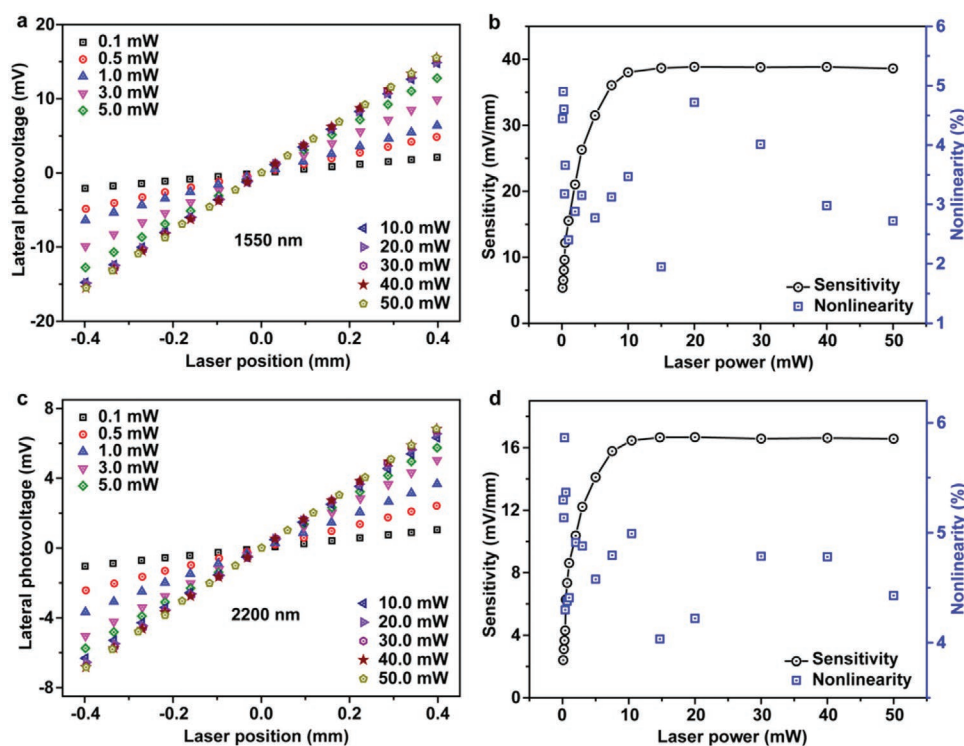


**Figure 4.** LPV curves under different powers illumination of a) 1550 and c) 2200 nm lasers, respectively. The extracted power-dependent sensitivities and nonlinearities for b) 1550 nm and d) 2200 nm, respectively.

$\kappa$  depends on both the carrier lifetime ( $\tau$ ) and the recombination rate ( $\xi$ ) with the expression of  $\kappa = 1 - \xi^{\beta\tau P/N_0}$  ( $\beta$  represents a wavelength-independent weight factor). Adding  $N_0$  and  $\kappa$  into the Equation (2), the sensitivity is rewritten as follows<sup>[46,49]</sup>

$$\text{Sensitivity} = \frac{2\kappa}{l_0} \left( \frac{P\lambda}{hc} \right)^\delta \exp\left(-\frac{L}{l_0}\right) \left( 1 - \xi^{\beta\tau(hc)^\delta P^{1-\delta}/\kappa\lambda^\delta} \right) \quad (3)$$

The sensitivity curves can be well fitted by using Equation (3), as shown in the red solid lines in Figure 3b,e. The best fitting  $\tau$  (averaged) is  $\approx 8.95 \times 10^{-6}$  s and  $\approx 1.63 \times 10^{-8}$  s for the 532 and the 1064 nm, respectively, which is comparable to the previous reported results.<sup>[47–49]</sup> More importantly, this result directly confirms that the sensitivity changing difference between the 532 and the 1064 nm in high powers should indeed result from the various carrier lifetimes of the Si substrate and the  $\text{Bi}_2\text{Te}_{2.7}\text{Se}_{0.3}$  layer due to their significant effect in the LPE.

It seems that the LPVs are all linearly dependent on the laser position, but there are more or less deviations from the ideal curves. To precisely identify their linear relationships, nonlinearity, as another key factor of a PSD, is also evaluated by the following equation<sup>[33,34]</sup>

$$\text{Nonlinearity (\%)} = \frac{2 \times \sqrt{\left[ \sum_{i=1}^n (LPV_i - LPV_i^L)^2 \right] / n}}{2L} \times 100\% \quad (4)$$

where  $n$  is the number of effective measuring points,  $LPV_i^L$  and  $LPV_i$  represent the linear fitted and measured LPV at the  $i$  point. Figure 3c,f gives the calculated nonlinearities for the 532 and the 1064 nm, respectively. It is clear that the nonlinearities (fluctuating at  $\approx 2.6\%$ ) are all much lower than the acceptable factor of 15%<sup>[34]</sup> and there is nearly no difference for the 532 and the 1064 nm, all of which may be attributed to the large carrier diffusion distance of the  $\text{Bi}_2\text{Te}_{2.7}\text{Se}_{0.3}$  layer due to its high surface mobility.<sup>[30,51]</sup> However, considering the relatively small LPE response, the background noise plays a relatively important effect, thus the nonlinearities of the 1550 nm ( $\approx 3.5\%$ ) and the 2200 nm ( $\approx 4.7\%$ ) are a little larger than that of the 532 or the 1064 nm, as shown in Figure 4b,d.

Notably, the  $\text{Bi}_2\text{Te}_{2.7}\text{Se}_{0.3}/\text{Si}$  heterojunction exhibits an unprecedented LPE response as the saturated sensitivity of  $283.71 \text{ mV mm}^{-1}$  at the 532 nm is among the best results ( $\approx 300 \text{ mV mm}^{-1}$ ) in the visible range,<sup>[40,41,43–46,52,53]</sup> and the sensitivity of  $137.4 \text{ mV mm}^{-1}$  at the 1064 nm nearly outshines any results (with the maximum of  $\approx 80 \text{ mV mm}^{-1}$  at 808 nm) reported till now in the infrared range.<sup>[45,46,49,54–56]</sup> More importantly, it is unprecedented that the LPE response is observed at the 1550 and 2200 nm, and meanwhile the sensitivities are also very considerable. These results demonstrate that the  $\text{Bi}_2\text{Te}_{2.7}\text{Se}_{0.3}/\text{Si}$  heterojunction shows a bright prospect in ultra-broadband infrared PSDs.

Besides the carrier lifetime, the barrier height is thought to be another critical parameter to determine the LPE response, as demonstrated by the thickness-dependent results shown in Figure 2f. From the previous results, many different methods have been successfully used to improve the barrier height, but adding a longitudinal external bias voltage is suggested to be a

simple and efficient method to modulate the band structure of the  $\text{Bi}_2\text{Te}_{2.7}\text{Se}_{0.3}/\text{Si}$  heterojunction.<sup>[21,22,57,58]</sup> Therefore, the bias effect on the LPE response is well studied in this heterojunction. Figures S4a,d and S5a,d, Supporting Information give the LPV results of the 532, 1064, 1550, and 2200 nm, respectively, with a 5 mW illumination and at different voltages (with measurement diagram shown in Figure 5a). The LPE response improves clearly with bias adding from 0 V to  $-1$  V, and the extracted sensitivity enhances from  $164.7 \text{ mV mm}^{-1}$  ( $/96.77 \text{ mV mm}^{-1}/31.43 \text{ mV mm}^{-1}/14.11 \text{ mV mm}^{-1}$ ) to  $320.5 \text{ mV mm}^{-1}$  ( $/171.5 \text{ mV mm}^{-1}/50.83 \text{ mV mm}^{-1}/23.12 \text{ mV mm}^{-1}$ ) for 532, 1064, 1550, and 2200 nm, respectively, with a maximal improvement of 194.6%, as shown in Figures S4b,e and S5b,e, Supporting Information. Obviously, there exists an ultimate voltage, above which the LPV response nearly keeps constant, and the ultimate voltage decreases from  $\approx -0.60$  to  $\approx -0.20$  V with wavelength increasing from 532 to 2200 nm, which is in accordance with the previous results.<sup>[59,60]</sup> Then, we also measured the LPV curves under illumination of 10 mW and 20 mW to well illustrate the effect of the bias, as shown in Figures S6 and S7, Supporting Information. When the power improves from 5 mW to 10 mW or 20 mW, the sensitivity also enhances with increasing bias voltage but with gradually slow growing rate as compared with that of 5 mW, indicating the limited separation capability of each bias voltage for a constant power illumination, therefore the ultimate voltage gets larger with increasing powers correspondingly, as shown in Figures S4b,e and S5b,e, Supporting Information.<sup>[59,60]</sup> However, this heterojunction still keeps very good linearity nearly without depending on the amplitude of the bias (Figures S4c,f and S5c,f, Supporting Information).

To understand the enhanced LPE response and effective bias modulation in the  $\text{Bi}_2\text{Te}_{2.7}\text{Se}_{0.3}/\text{Si}$  heterojunction, the energy-band diagrams are proposed and well analyzed. From the previous results, the electron affinities of Si and  $\text{Bi}_2\text{Te}_{2.7}\text{Se}_{0.3}$  are  $\approx 4.05$  eV and  $\approx 4.35$  eV, respectively,<sup>[21,22,28]</sup> leading to a conduction band offset of  $\approx 0.25$  eV when preparing the  $\text{Bi}_2\text{Te}_{2.7}\text{Se}_{0.3}$  layer on the Si substrate. Then, dominated by the 0.25 eV negative conduction band edge of the  $\text{Bi}_2\text{Te}_{2.7}\text{Se}_{0.3}$  layer, electrons would diffuse from the Si into the  $\text{Bi}_2\text{Te}_{2.7}\text{Se}_{0.3}$  and holes diffuse inversely, thus the energy bands in the  $\text{Bi}_2\text{Te}_{2.7}\text{Se}_{0.3}$  and Si bend downward and upward, respectively, and a barrier is produced in the interface, as shown in Figure 5b. When a light (with enough energy to generate the Si or the  $\text{Bi}_2\text{Te}_{2.7}\text{Se}_{0.3}$  layers) illuminates on the heterojunction, electron–hole pairs would be excited in the  $\text{Bi}_2\text{Te}_{2.7}\text{Se}_{0.3}$  layer or both the  $\text{Bi}_2\text{Te}_{2.7}\text{Se}_{0.3}$  and the Si layers, then these carriers are swept away by the interface field into the Si or  $\text{Bi}_2\text{Te}_{2.7}\text{Se}_{0.3}$  layer, as shown in Figure 5c. Although the number of the photo-induced carriers increases gradually by adding light intensity, the separated and transmitted carriers are so limited due to their slow transmitting velocity and fast recombination rate. When an external bias is added on the device, the energy bands of the Si would further go downward, so that the depletion region as well as the barrier height is improved, as shown in Figure 5d. Therefore, these carriers are more easily swept away by the enhanced field and quickly transmitted into the  $\text{Bi}_2\text{Te}_{2.7}\text{Se}_{0.3}$  and the Si layers.<sup>[21,22]</sup> However, considering the unavoidable annihilation or recombination, there is an ultimate voltage for each power, above which the LPE would reach to an optimal response and nearly keep constant.<sup>[59,60]</sup>

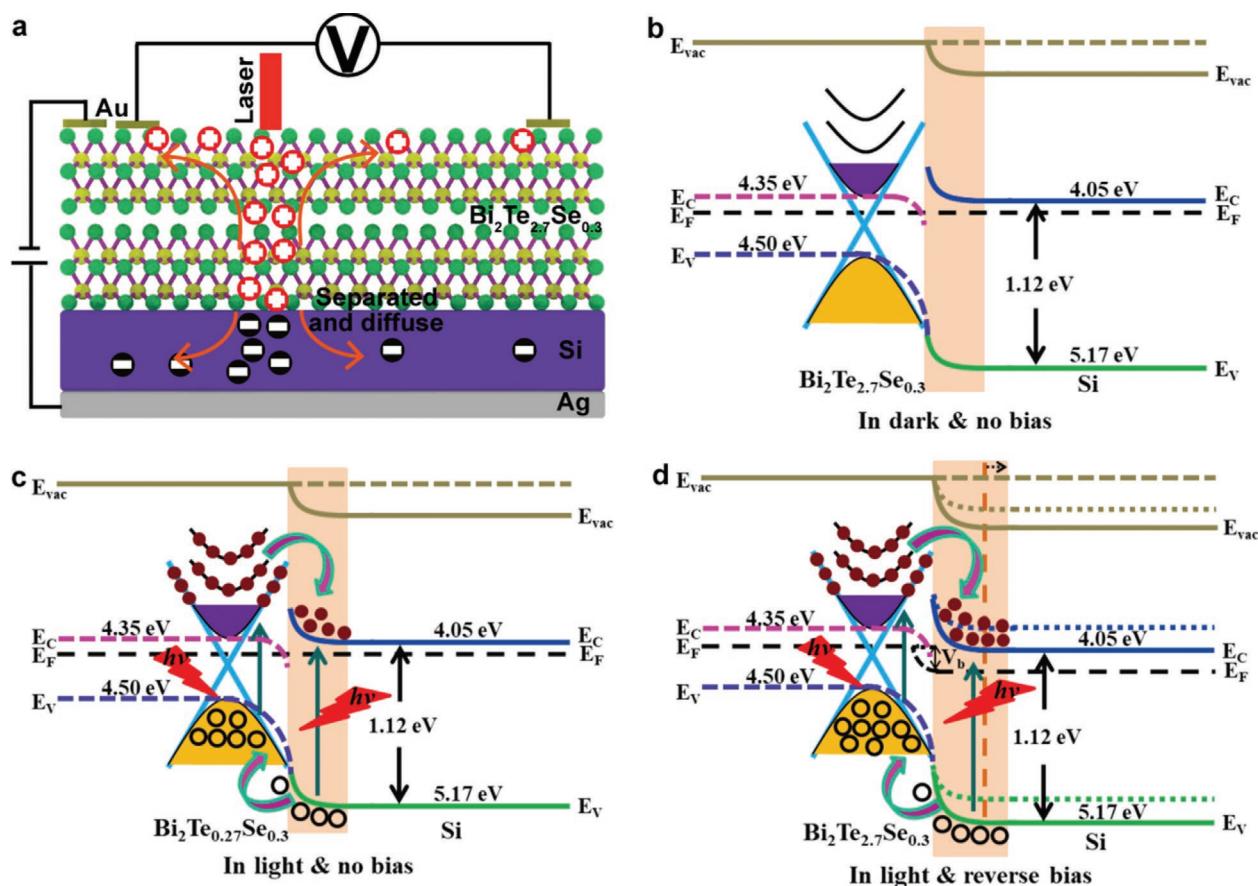


**Figure 5.** a) LPV measurement diagram with adding a bias voltage. The energy band diagrams of the  $\text{Bi}_2\text{Te}_{2.7}\text{Se}_{0.3}/\text{Si}$  heterojunction b) in dark, c) in light without bias voltage, and d) in light with bias voltage.

At last, the response speed, as another key parameter of a photodetector,<sup>[34,61]</sup> is also well studied in the  $\text{Bi}_2\text{Te}_{2.7}\text{Se}_{0.3}/\text{Si}$  heterojunction. During the measurement, a linear motor stage is utilized to control the sample position, and a continuous wave (CW) laser modulated with a mechanical chopper is used to illuminate the sample, then the time-dependent lateral photovoltage (LPV-t) curve (under periodic laser on and off illumination) can be generated and recorded by an oscilloscope. **Figure 6a** gives a typical LPV-t curve for a 532 nm illumination. There is no obvious attenuation and oscillation in the measured region of  $\approx 40$  cycles, indicating the excellent photoresponse repeatability and stability of this heterojunction. However, an instantaneous LPV peak can be surprisingly observed at the laser on stage, which may be attributed to the pyro-phototronic effect.<sup>[62–66]</sup> Firstly, the LPV-t curves were identified under different power illuminations of a 532 nm laser at 1000 Hz with laser beam staying at  $x = 0.36$  mm, as shown in **Figure 6b**. Obviously, the instantaneous LPV peak improves with increasing illumination power, but the steady-state LPV values (after laser on stage) are still the same as that of the laser position-dependent LPV results (**Figure 3a**) at corresponding laser position and powers, implying its fast response speed. **Figure 6c** gives the laser power-dependent response times (rise and fall), which are extracted by evaluating the time interval between 10% and 90% of the LPV amplitude at rising and falling edges.

The rise time increases from  $\approx 55.7$  to  $\approx 72.4$   $\mu\text{s}$  with laser power changing from 50 to 0.5 mW, but the fall time nearly keeps at  $\approx 79.5$   $\mu\text{s}$  except the low illumination powers of 0.5 and 1.0 mW, which may result from the laser power-dependent pyro-phototronic effect. However, for traditional photodetectors, the pyro-phototronic effect usually improves both the rise and the fall times,<sup>[62–66]</sup> which is inconsistent with our results. To well understand this phenomenon, we also divided the time-dependent LPV curve into four stages (as shown in **Figure 7a**) and analyzed the working mechanisms of this PSD. There are two processes for the photo-generated carriers in the LPE. When a laser is suddenly turned on and illuminated on the  $\text{Bi}_2\text{Te}_{2.7}\text{Se}_{0.3}$  film, a pyroelectric potential is immediately generated in longitudinal direction due to a temperature increase, then the potential field would weaken the downward bending of the conduction band (as shown in **Figure 5c**), resulting in more photo-excited electrons easily sweeping away from the  $\text{Bi}_2\text{Te}_{2.7}\text{Se}_{0.3}$  layer, hence the number of the separated holes is increased (as compared with that of the steady-state stage), as shown in **Figure 7b**. Therefore, the instantaneous LPV, which is dominated by both the photoelectric effect (normal diffusion) and the pyro-phototronic effect ( $dT/dt$  enhanced diffusion), is improved (called as  $\text{LPV}_{\text{pyro+photo}}$ ) as compared with that induced only by the photoelectric effect (called as  $\text{LPV}_{\text{photo}}$ ). Though there are also two different transverse temperature gradients on

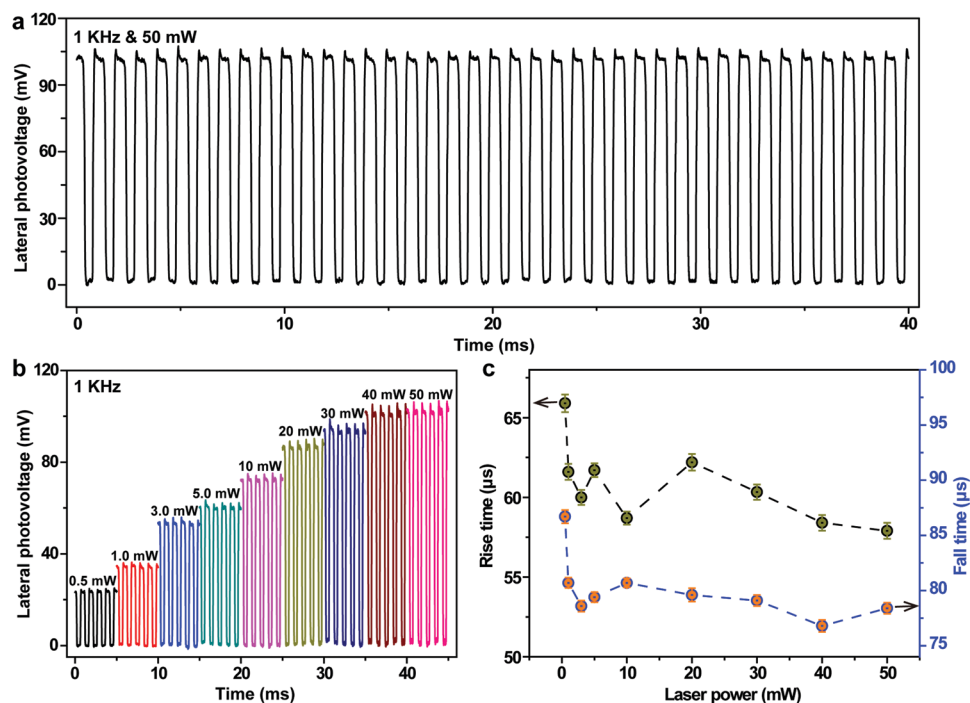


**Figure 6.** a) t-LPV curve under 50 mW illumination of a 532 nm laser at 1000 Hz. b) t-LPV curves of different powers illumination. c) The extracted response times as a function of illumination power.

both sides of the laser beam,<sup>[67,68]</sup> which can accelerate the diffusion of these holes to the Au electrodes, but this contribution is very small and the gradient keeps always in the illumination stage. After a short moment (Stage II), the temperature distribution gets balanced and the pyroelectric potential falls away quickly, then only the initial interface field can be used to separate the carriers, thus the LPV gradually reduces from a transient LPV<sub>pyro+photo</sub> to a stable LPV<sub>photo</sub>, as shown in Figure 7c. When suddenly turning off the laser (Stage III), a temperature decrease is instantaneously happened, resulting in an opposite longitudinal pyroelectric potential (as compared with stage I), as shown in Figure 7d. However, here the potential has no effect on the LPE response because of the disappearance of the photo-generated carriers. At last, the temperature returns back and keeps constant as room temperature (Stage VI), so that the pyroelectric potential is disappeared, and the LPV still keeps at zero in this stage (Figure 7e). With decreasing the laser power, the instantaneous temperature changing decreases accompanied by the weakened pyro-phototronic effect and the decreased rising peak of the LPV (as shown in Figure 6b). To further testify the pyro-phototronic effect in this heterojunction, we also prepared this heterostructure as a PD and measured the transient photoresponse, as shown in Figure S8, Supporting Information. The photocurrent peak appears at both the laser on and the laser off stages, which is very similar to that observed in other systems induced by the pyro-phototronic effect.<sup>[62–66]</sup>

Moreover, it is suggested that a faithful PSD should exhibit a wide bandwidth to make it collect a reliable optical signal over the entire bandwidth and the response speed obtained at high pulse frequencies may be more accuracy due to the longer time taken on the laser on stage at low frequencies.<sup>[55]</sup> Then, to evaluate the bandwidth and frequency response of

the Bi<sub>2</sub>Te<sub>2.7</sub>Se<sub>0.3</sub>/Si heterojunction PSD, the LPV-t curves are measured under illumination of 50 mW of a 532 nm laser with chopper frequency changing from 50 to 4000 Hz, as shown in Figure 8a,b. The steady-state LPV nearly keeps constant in the whole frequency range, indicating the wide frequency response range and the ultrafast optical detecting capability of this heterojunction. However, the instantaneous rising peak is strongly dependent on the laser frequency as there is no clear peaks observed in low frequencies, and the instantaneous LPV peak starts to appear when the frequency is larger than ≈200 Hz, and enhances with increasing the frequency, demonstrating the fast temperature variation speed and the slow laser on or off speed (the temperature can quickly achieve a balance due to the longer laser on or off time in low frequencies; with increasing frequency, the laser on or off time gets increasingly short, so that the temperature changing starts to form and improves accordingly). Moreover, this phenomenon further confirms the important effect of frequency or pulse width on the response speed (the response speed may be slowed down by the long laser on or off times).<sup>[50,65]</sup> Figure 8c shows the frequency-dependent rise and fall times.<sup>[50,65]</sup> The response time decreases quickly from ≈1050 μs/≈1140 μs to ≈58.3 μs/≈80 μs with pulse frequency increasing from 50 to 1000 Hz, and then decreases slightly from ≈54.5 μs/≈70.4 μs to ≈52.1 μs/≈70.2 μs with frequency changing from 2000 to 4000 Hz. Obviously, the large response times in low frequencies are resulted from both the slow laser on or off speed (with long pulse width) and the large sampling bandwidth of the oscilloscope (with low time resolution), while the slightly decreased rise time in high frequencies can be mainly attributed to the improved pyro-phototronic effect.

Previously, it has been reported that the laser position has no effect on the response speed, but there is no

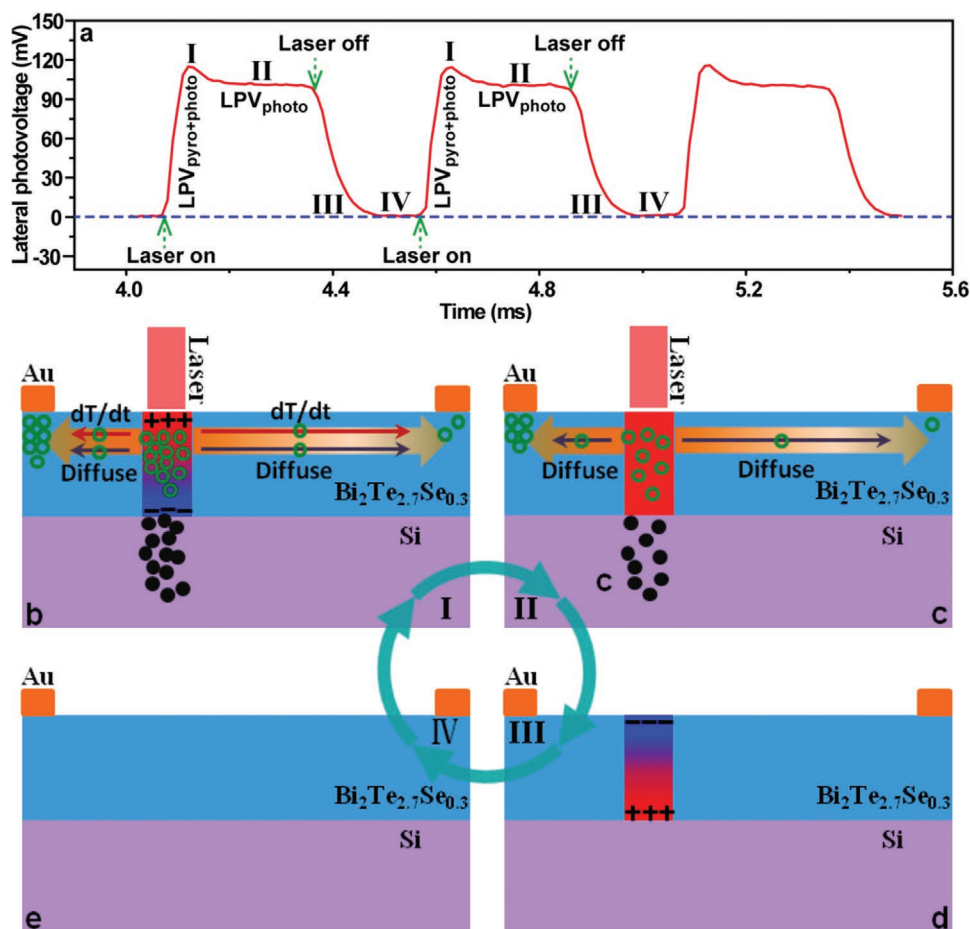


**Figure 7.** a) An enlarged t-LPV curve labeled as four stages (I, II, III, IV). b) Working mechanism illustration of LPE and pyroelectric effect at stage b) I, c) II, d) III, and e) IV, respectively.

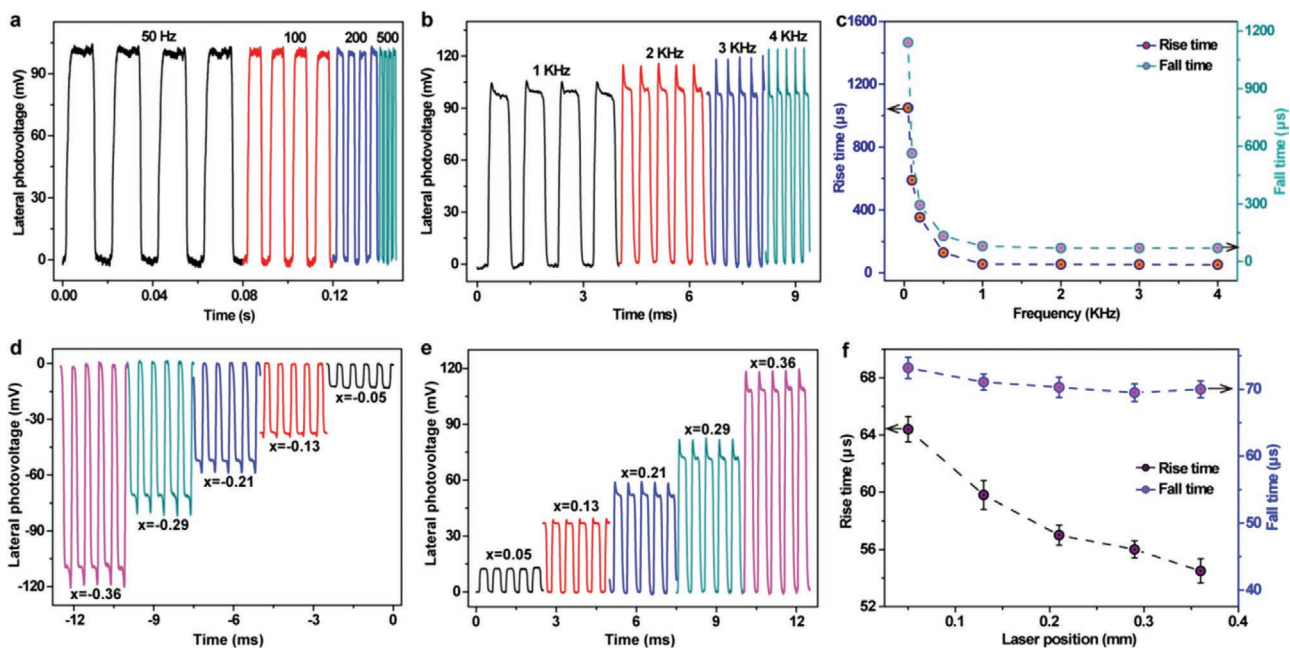


**Figure 8.** a, b) t-LPV curves under 50 mW illumination of a 532 nm laser at different frequencies. c) The extracted response times as a function of frequency. d, e) t-LPV curves of different laser positions at 2000 Hz. f) The extracted response times as a function of laser position.

pyro-phototronic effect observed in these systems.<sup>[46]</sup> Therefore, to evaluate whether the response time depends on the laser position or not in this heterojunction, the LPV-t curves were also measured with laser staying at ten different positions under illumination of 50 mW at 2000 Hz, with results shown in Figure 8d,e. The steady-state LPVs are also the same as that of the corresponding LPV results shown in Figure 3a, but the instantaneous LPV peak decreases with laser position moving from  $\pm 0.36$  to  $\pm 0.05$  mm due to the decreased diffusion difference of the separated carriers in the right and the left sides of the laser position. Dominated mainly by the laser position-dependent pyro-phototronic effect, the rise and fall time increases gradually from  $\approx 54.5$  to  $\approx 64.4$   $\mu\text{s}$  and slightly from  $\approx 70.4$  to  $\approx 71.8$   $\mu\text{s}$  with laser position changing from  $\pm 0.36$  to  $\pm 0.05$  mm, respectively, as shown in Figure 8f (considering nearly the same steady-state LPVs and response speeds at the laser positions with centric symmetry, we only plot the laser position-dependent rise and fall times at the positive positions but calculating their errors together). At last, to further study the pyro-phototronic effect and illustrate the dependence of response speed on the laser wavelength, the LPV-t curves are studied under illumination of different lasers and at different bias voltages, as shown in Figure S9a,c, Supporting Information, respectively. From Figure S9a, Supporting Information, it is clear that the steady-state LPV reduces with increasing laser wavelength, while the instantaneous LPV peak nearly keeps constant, further demonstrating that the pyro-phototronic effect is mainly dependent on the laser power (temperature changing). The response times are calculated and summarized in Figure S9b, Supporting Information. The fall time still keeps at  $\approx 70$   $\mu\text{s}$  but the rise time greatly improves from  $\approx 54.5$   $\mu\text{s}$  to  $\approx 38.7$   $\mu\text{s}$  with wavelength increasing from 532 to 2200 nm. Figure S9c, Supporting Information gives the LPV-t curves of different biases ranging from 0 V to  $-1$  V. As the bias-modulated LPE responses in Figure S4a, Supporting Information, the steady-state LPV also enhances correspondingly. However, the instantaneous LPV peak decreases quickly with increasing bias and nearly vanishes when it is above  $\approx -0.5$  V. This can also be well understood as the longitudinal pyro-phototronic effect can be weakened by the increased background temperature due to the large dark currents for higher bias voltages. Moreover, the field of the bias can decelerate the back tunneling of the separated carriers.<sup>[51,60]</sup> Therefore, dominated by the bias voltage-dependent longitudinal carrier modulation, the rise time decreases from  $\approx 58.1$  to  $\approx 49.7$   $\mu\text{s}$  while the fall time increases from  $\approx 70.2$  to  $\approx 85.6$   $\mu\text{s}$  as the bias changes from 0 V to  $-1$  V, as shown in Figure S9d, Supporting Information.

### 3. Conclusion

In conclusion, a series of  $\text{Bi}_2\text{Te}_{2.7}\text{Se}_{0.3}$  films are successfully prepared on the Si substrate with *c*-axis preferred orientation to form the high-quality  $\text{Bi}_2\text{Te}_{2.7}\text{Se}_{0.3}/\text{Si}$  heterojunctions. The heterojunctions exhibit an unprecedentedly ultrabroadband response at least ranging from  $\approx 350$  to  $\approx 2200$  nm and the heterojunction PSDs can work normally without any external power. Dominated by the thickness-dependent depletion layer width and diffusion length, the LPE response of this heterojunction

has an optimal  $\text{Bi}_2\text{Te}_{2.7}\text{Se}_{0.3}$  layer thickness of  $\approx 10$  nm. LPE measurements suggest that the  $\text{Bi}_2\text{Te}_{2.7}\text{Se}_{0.3}$  (10 nm)/Si heterojunction PSD exhibits very high performances with ultralarge sensitivity (283.71  $\text{mV mm}^{-1}$ , 137.4  $\text{mV mm}^{-1}$ , 38.91  $\text{mV mm}^{-1}$ , and 16.56  $\text{mV mm}^{-1}$  at 532, 1064, 1550, and 2200 nm, respectively), very good linearity, and ultrafast response speed ( $\approx 52.1$   $\mu\text{s}/\approx 70.2$   $\mu\text{s}$ ), which can be attributed to the strong and broadband absorption, high surface mobility of the  $\text{Bi}_2\text{Te}_{2.7}\text{Se}_{0.3}$  layer and the excellent heterojunction. Moreover, the LPE response can be largely modulated with adding a bias voltage because of the enhanced built-in field. Additionally, the pyro-phototronic effect is observed in this heterojunction, which can improve the rise speed but have no effect on the fall time due to the different working mechanisms as the traditional photodetectors. This work paves the way for designing and developing high-performance ultrabroadband infrared PSDs by utilizing the synergetic effect of the Si semiconductor and the topological insulators as well as the pyro-phototronic effect.

### 4. Experimental Section

*Preparation of the  $\text{Bi}_2\text{Te}_{2.7}\text{Se}_{0.3}$  Films and Devices:* A series of Se-doped  $\text{Bi}_2\text{Te}_3$  samples with thicknesses of 5, 7, 10, 20 nm and 30, 40, 50 nm were prepared by using pulsed-laser deposition (PLD) technology on the n-type Si (100) substrates. The PLD target material was synthesized by mixing the high-purity Te (99.999%), Bi (99.999%), and Se (99.999%) raw powders together with the nominal Se-dopant component of  $\text{Bi}_2\text{Te}_{2.7}\text{Se}_{0.3}$ . The thickness and the resistivity of the Si substrate was  $\approx 500$   $\mu\text{m}$  and  $\approx 10$   $\Omega\text{-cm}$  (at 298 K), respectively. Before loading into the deposition chamber, the Si wafers were carefully treated. During the deposition, a pulsed XeCl ( $\lambda = 308$  nm) excimer laser was used with a rate of 5 Hz and an intensity of 1.2  $\text{J cm}^{-2}$ ; the base chamber pressure was better than  $5.0 \times 10^{-5}$  Pa, and the substrate temperature and depositing pressure was kept at 300  $^\circ\text{C}$  and 40 Pa, respectively, with Ar flow rate of 25 standard cubic centimeters per minute (SCCM). The preparation rate was about 5  $\text{nm min}^{-1}$ , so that by controlling the preparation time, different thickness films can be obtained. After preparation, two Au (50 nm-thickness) point electrodes with distance of 0.8 mm were deposited on the  $\text{Bi}_2\text{Te}_{2.7}\text{Se}_{0.3}$  film by thermal evaporation controlling with a metal mask.

*Characterizations and Measurements of the  $\text{Bi}_2\text{Te}_{2.7}\text{Se}_{0.3}/\text{Si}$  Heterojunction:* The crystal structure, crystal quality, morphology, and elementary composition of the  $\text{Bi}_2\text{Te}_{2.7}\text{Se}_{0.3}$  films are identified by XRD (Bruker, D8 Advance), HRTEM (FEI, Tecnai G2 F20S-TWIN), Raman (Horiba, LabRAM HR Evolution), SEM (FEI, Nova NanoSE M450), and EDXS (OCTANE PLUS). The LPV curves are identified by combing a Keithley 2700 voltmeter and a 3D linear motor stage with a laser perpendicularly illuminating on the sample simultaneously. The LPV-t curves are characterized by using a chopper-modulated pulse laser and a digital oscilloscope (Agilent DSO X 4022A). The I-V responses are evaluated with a Keithley 2400 SourceMeter.

### Supporting Information

Supporting Information is available from the Wiley Online Library or from the author.

### Acknowledgements

This work is supported by the National Nature Science Foundation of China (Grant Nos. 11704094, 11504076, 51372064, 61405040, 51622205,

61675027, 51432005, and 61505010), the Nature Science Foundation of Hebei Province (Grant Nos. F2019201047, E2017201227, F2017201141, and F2018201198), the Science and Technology Research Project of Hebei Province Higher Education Institution (Grant No. ZD2016036), Nature Science Foundation for Distinguished Young Scholars of Hebei University (Grant No. 2015JQ03), the Young Talents of Hebei Province, the support of National Key R & D Project from Minister of Science and Technology (2016YFA0202703).

## Conflict of Interest

The authors declare no conflict of interest.

## Keywords

lateral photovoltaic effect, position sensitive detector, pyro-phototronic effect, TI heterostructures

Received: July 25, 2019

Revised: August 27, 2019

Published online:

- [1] H. Zhang, C. X. Liu, X. L. Qi, X. Dai, Z. Fang, S. C. Zhang, *Nat. Phys.* **2009**, *5*, 438.
- [2] M. Z. Hasan, C. L. Kane, *Rev. Mod. Phys.* **2010**, *82*, 3045.
- [3] X. L. Qi, S. C. Zhang, *Rev. Mod. Phys.* **2011**, *83*, 1057.
- [4] C. Z. Chang, J. S. Zhang, X. Feng, J. Shen, Z. C. Zhang, M. H. Guo, K. Li, Y. B. Ou, P. Wei, L. L. Wang, Z. Q. Ji, Y. Feng, S. H. Ji, X. Chen, J. F. Jia, X. Dai, Z. Fang, S. C. Zhang, K. He, Y. Y. Wang, L. Lu, X. C. Ma, Q. K. Xue, *Science* **2013**, *340*, 167.
- [5] M. Jamali, J. S. Lee, J. S. Jeong, F. Mahfouzi, Y. Lv, Z. Y. Zhao, B. K. Nikolic, K. A. Mkhoyan, N. Samarth, J. P. Wang, *Nano Lett.* **2015**, *15*, 7126.
- [6] Y. Xia, D. Qian, D. Hsieh, L. Wray, A. Pal, H. Lin, A. Bansil, D. Grauer, Y. S. Hor, R. J. Cava, M. Z. Hasan, *Nat. Phys.* **2009**, *5*, 398.
- [7] D. Kong, Y. Cui, *Nat. Chem.* **2011**, *3*, 845.
- [8] X. Zhang, J. Wang, S. C. Zhang, *Phys. Rev. B* **2010**, *82*, 245107.
- [9] Z. Alpichshev, J. G. Analytis, J. H. Chu, I. R. Fisher, Y. L. Chen, Z. X. Shen, A. Fang, A. Kapitulnik, *Phys. Rev. Lett.* **2010**, *104*, 016401.
- [10] Y. H. Wang, D. Hsieh, D. Pilon, L. Fu, D. R. Gardner, Y. S. Lee, N. Gedik, *Phys. Rev. Lett.* **2011**, *107*, 207602.
- [11] J. A. Sobota, S. Yang, J. G. Analytis, Y. L. Chen, I. R. Fisher, P. S. Kirchmann, Z. X. Shen, *Phys. Rev. Lett.* **2012**, *108*, 117403.
- [12] M. Hajlaoui, E. Papalazarou, J. Mauchain, G. Lantz, N. Moisan, D. Boschetto, Z. Jjiang, I. Miotkowski, Y. P. Chen, A. Taleblabrahimi, L. Perfetti, M. Marsi, *Nano Lett.* **2012**, *12*, 3532.
- [13] H. Qiao, J. Yuan, Z. Q. Xu, C. Y. Chen, S. H. Lin, Y. S. Wang, J. C. Song, Y. Liu, Q. Khan, H. Y. Hoh, C. X. Pan, S. J. Li, Q. L. Bao, *ACS Nano* **2015**, *9*, 1886.
- [14] J. Kim, S. Park, H. Jang, N. Koirala, J. B. Lee, U. J. Kim, H. S. Lee, Y. G. Roh, H. Lee, S. W. Sim, S. Y. Cha, C. In, J. Park, J. Lee, M. Noh, J. Moon, M. Salehi, J. Sung, S. S. Chee, M. H. Ham, M. H. Jo, S. Oh, J. H. Ahn, S. W. Hwang, D. Kim, H. Choi, *ACS Photon.* **2017**, *4*, 482.
- [15] J. D. Yao, Z. Q. Zheng, G. W. Yang, *Adv. Funct. Mater.* **2017**, *27*, 1701823.
- [16] J. D. Yao, Z. Q. Zheng, G. W. Yang, *J. Mater. Chem. C* **2016**, *4*, 7831.
- [17] Z. Q. Zeng, T. A. Morgan, D. S. Fan, C. Li, Y. Hirono, X. Hu, Y. F. Zhao, J. S. Lee, J. Wang, Z. M. Wang, S. Q. Yu, M. E. Hawkrige, M. Benamara, G. J. Salamo, *AIP Adv.* **2013**, *3*, 072112.
- [18] Q. K. Wang, X. H. Wu, L. M. Wu, Y. J. Xiang, *AIP Adv.* **2019**, *9*, 025022.
- [19] J. Zang, Z. P. Peng, A. Soni, Y. Y. Zhao, Y. Xiong, B. Peng, J. B. Wang, M. S. Dresselhaus, Q. H. Xiong, *Nano Lett.* **2011**, *11*, 2407.
- [20] Y. Y. Li, G. Wang, X. G. Zhu, M. H. Liu, C. Ye, X. Chen, Y. Y. Wang, K. He, L. L. Wang, X. C. Ma, H. J. Zhang, X. Dai, Z. Fang, X. C. Xie, Y. Liu, X. L. Qi, J. F. Jia, S. C. Zhang, Q. K. Xue, *Adv. Mater.* **2010**, *22*, 4002.
- [21] J. D. Yao, J. M. Shao, Y. X. Wang, Z. R. Zhao, G. W. Yang, *Nanoscale* **2015**, *7*, 12535.
- [22] H. B. Zhang, X. J. Zhang, C. Liu, S. T. Lee, J. S. Jie, *ACS Nano* **2016**, *10*, 5113.
- [23] C. Liu, H. B. Zhang, Z. Sun, K. Ding, J. Mao, Z. B. Shao, J. S. Jie, *J. Mater. Chem. C* **2016**, *4*, 5648.
- [24] Z. H. Wang, M. Z. Li, L. Yang, Z. D. Zhang, X. P. A. Gao, *Nano Res.* **2017**, *10*, 1872.
- [25] B. Das, N. S. Das, S. Sarkar, B. K. Chatterjee, K. K. Chattopadhyay, *ACS Appl. Mater. Interfaces* **2017**, *9*, 22788.
- [26] J. J. Liu, Y. Y. Li, Y. X. Song, Y. J. Ma, Q. M. Chen, Z. Y. S. Zhu, P. F. Lu, S. M. Wang, *Appl. Phys. Lett.* **2017**, *110*, 141109.
- [27] A. Parbatani, E. S. Song, F. Yang, B. Yu, *Nanoscale* **2018**, *10*, 15003.
- [28] C. O. Aristizabal, M. S. Fuhrer, N. P. Butch, J. Paglione, I. Appelbaum, *Appl. Phys. Lett.* **2012**, *101*, 023102.
- [29] H. D. Li, L. Gao, H. Li, G. Y. Wang, J. Wu, Z. H. Zhou, Z. M. Wang, *Appl. Phys. Lett.* **2013**, *102*, 074106.
- [30] J. N. Hancock, J. L. M. van Mechelen, A. B. Kuzmenko, D. van der Marel, C. Brüne, E. G. Novik, G. V. Astakhov, H. Buhmann, L. W. Molenkamp, *Phys. Rev. Lett.* **2011**, *107*, 136803.
- [31] H. Peng, W. Dang, J. Cao, Y. Chen, D. Wu, W. Zheng, H. Li, Z. X. Shen, Z. Liu, *Nat. Chem.* **2012**, *4*, 281.
- [32] R. Martins, E. Fortunato, *Rev. Sci. Instrum.* **1995**, *66*, 2927.
- [33] J. Henry, J. Livingstone, *Adv. Mater.* **2001**, *13*, 1022.
- [34] E. Fortunato, G. Lavareda, R. Martins, F. Soares, L. Fernandes, *Sens. Actuators, A* **1995**, *51*, 135.
- [35] W. Richter, C. R. Becker, *Phys. Status Solidi (b)* **1977**, *84*, 619.
- [36] Y. Xiang, X. Dai, S. Wen, *Appl. Phys. A* **2007**, *87*, 285.
- [37] Q. You, Y. X. Shan, S. W. Gan, Y. T. Zhao, X. Y. Dai, Y. J. Xiang, *Opt. Mater. Express* **2018**, *8*, 3036.
- [38] L. M. Wu, J. Guo, H. L. Xu, X. Y. Dai, Y. J. Xiang, *Photon. Res.* **2016**, *4*, 262.
- [39] C. Q. Yu, H. Wang, S. Q. Xiao, Y. X. Xia, *Opt. Express* **2009**, *17*, 21712.
- [40] C. Q. Yu, H. Wang, Y. X. Xia, *Appl. Phys. Lett.* **2009**, *95*, 263506.
- [41] S. Qiao, J. H. Chen, J. H. Liu, N. Fu, G. Y. Yan, S. F. Wang, *Appl. Surf. Sci.* **2015**, *356*, 732.
- [42] C. Wang, K. J. Jin, R. Q. Zhao, H. B. Lu, H. Z. Guo, C. Ge, M. He, C. Wang, G. Z. Yang, *Appl. Phys. Lett.* **2011**, *98*, 181101.
- [43] C. Q. Yu, H. Wang, *Appl. Phys. Lett.* **2010**, *96*, 171102.
- [44] J. H. Liu, S. Qiao, B. L. Liang, S. F. Wang, G. S. Fu, *Opt. Express* **2017**, *25*, A166.
- [45] X. J. Wang, X. F. Zhao, C. Hu, Y. Zhang, B. Q. Song, L. L. Zhang, W. L. Liu, Z. Lv, L. Zhang, J. K. Tang, Y. Sui, B. Song, *Appl. Phys. Lett.* **2016**, *109*, 023502.
- [46] S. Qiao, K. Y. Feng, Z. Q. Li, G. S. Fu, S. F. Wang, *J. Mater. Chem. C* **2017**, *5*, 4915.
- [47] M. Zhao, J. Zhang, N. Y. Gao, P. Song, M. Bosman, B. Peng, B. Q. Sun, C. W. Qiu, Q. H. Xu, Q. L. Bao, K. P. Loh, *Adv. Mater.* **2016**, *28*, 3138.
- [48] J. Zhao, Z. J. Xu, Y. Y. Zang, Y. Gong, X. Zheng, K. He, X. A. Cheng, T. Jiang, *Opt. Express* **2017**, *25*, 14635.
- [49] S. Qiao, B. Zhang, K. Y. Feng, R. D. Cong, W. Yu, G. S. Fu, S. F. Wang, *ACS Appl. Mater. Interfaces* **2017**, *9*, 18377.
- [50] R. D. Cong, S. Qiao, J. H. Liu, J. S. Mi, W. Yu, B. L. Liang, G. S. Fu, C. F. Pan, S. F. Wang, *Adv. Sci.* **2018**, *5*, 1700502.
- [51] J. H. Liu, S. Qiao, J. L. Wang, S. F. Wang, G. S. Fu, *Mater. Sci. Eng., B* **2017**, *218*, 1.

- [52] K. Zhao, K. J. Jin, H. B. Lu, Y. H. Huang, Q. L. Zhou, M. He, Z. H. Chen, Y. L. Zhou, G. Z. Yang, *Appl. Phys. Lett.* **2006**, *88*, 141914.
- [53] K. J. Jin, K. Zhao, H. B. Lu, L. Liao, G. Z. Yang, *Appl. Phys. Lett.* **2007**, *91*, 081906.
- [54] K. J. Jin, H. B. Lu, K. Zhao, C. Ge, M. He, G. Z. Yang, *Adv. Mater.* **2009**, *21*, 4636.
- [55] W. H. Wang, Z. Z. Yan, J. F. Zhang, J. P. Lu, H. Qin, Z. H. Ni, *Optica* **2018**, *5*, 27.
- [56] J. Lu, H. Wang, *Opt. Express* **2012**, *20*, 215502.
- [57] K. Zheng, L. B. Luo, T. F. Zhang, Y. H. Liu, Y. Q. Yu, R. Lu, H. L. Qiu, Z. J. Li, J. C. A. Huang, *J. Mater. Chem. C* **2015**, *3*, 9154.
- [58] W. S. Zheng, T. Xie, Y. Zhou, Y. L. Chen, W. Jiang, S. L. Zhao, J. X. Wu, Y. M. Jing, Y. Wu, G. C. Chen, Y. F. Guo, J. B. Yin, S. Y. Huang, H. Q. Xu, Z. F. Liu, H. L. Peng, *Nat. Commun.* **2015**, *6*, 6972.
- [59] S. Qiao, Y. N. Liu, J. H. Liu, J. H. Chen, G. Y. Yan, S. F. Wang, G. S. Fu, *Appl. Phys. Express* **2015**, *8*, 122201.
- [60] J. H. Liu, L. H. Zhang, Y. N. Liu, S. Qiao, G. Y. Yan, S. F. Wang, G. S. Fu, *Mater. Lett.* **2016**, *168*, 48.
- [61] C. Narayanan, A. B. Buckman, I. B. Vishniac, W. J. Wang, *IEEE Trans. Electron Devices* **1993**, *40*, 1688.
- [62] Z. N. Wang, R. M. Yu, C. F. Pan, Z. L. Li, J. Yang, F. Yi, Z. L. Wang, *Nat. Commun.* **2015**, *6*, 8401.
- [63] Z. N. Wang, R. M. Yu, X. F. Wang, W. Z. Wu, Z. L. Wang, *Adv. Mater.* **2016**, *28*, 6880.
- [64] W. B. Peng, X. F. Wang, R. M. Yu, Y. J. Dai, H. Y. Zou, A. C. Wang, Y. N. He, Z. L. Wang, *Adv. Mater.* **2017**, *29*, 1606698.
- [65] Y. J. Dai, X. F. Wang, W. B. Peng, C. Xu, C. S. Wu, K. Dong, R. Y. Liu, Z. L. Wang, *Adv. Mater.* **2018**, *30*, 1705893.
- [66] M. Kumar, M. Patel, J. Kim, B. Lim, *Nanoscale* **2017**, *9*, 19201.
- [67] S. Qiao, J. H. Liu, G. Y. Yan, J. H. Zhao, X. H. Zhang, S. F. Wang, G. S. Fu, *Appl. Phys. Lett.* **2015**, *107*, 182402.
- [68] B. S. Ouyang, K. W. Zhang, Y. Yang, *iScience* **2018**, *1*, 16.